

Application of Aerodynamic Shape Optimization to Swept Natural Laminar Flow Wings

Fizaa Husain*, Isabel Simmons†, David W. Zingg‡

Institute for Aerospace Studies, University of Toronto, Toronto, Ontario, M3H 5T6, Canada

The application of natural laminar flow has been limited to modest Reynolds numbers and sweep angles due to the effect of crossflow instabilities on boundary-layer transition for transonic swept-wing aircraft. In this paper a Reynolds-averaged Navier-Stokes based aerodynamic shape optimization framework coupled with the SA-sLM2015cc local correlation-based transition model is applied to lift-constrained drag minimization of infinite swept wings at the cruise conditions of business and regional jets and of a finite swept wing at the cruise conditions of a single-aisle aircraft. In the case of infinite swept wings, the optimizations achieve a profile drag reduction of 20% for the regional jet and 40% for the business jet, corresponding to estimated aircraft-level drag reductions of 5% and 10%, respectively, compared to an infinite swept wing optimized and analyzed under fully-turbulent conditions. This reduction is attributed to a combination of decreases in pressure drag and viscous drag resulting from the region of laminar flow on both surfaces. Furthermore, a multipoint optimization demonstrates the robustness of the optimized design to changes in Mach number and coefficient of lift. For the finite-wing optimization, there is a wing drag reduction of 21% compared to the baseline configuration and 10% compared to a wing optimized and analyzed under fully-turbulent conditions. The latter corresponds to an estimated aircraft-level drag reduction of 5%. Finally, the design space associated with lift-constrained drag minimization of a low-speed airfoil is studied with respect to multimodality. Two clearly distinct local minima are found with substantially different geometries and performance, indicating that multimodality may be a more significant issue when optimizing with laminar-turbulent transition prediction.

I. Introduction

THE aviation industry's environmental impact underscores the need for substantial efforts to improve aircraft efficiency. Projections indicate that the demand for air travel, measured in terms of scheduled passengers, will surge from 4.5 billion in 2019 to approximately 10 billion by 2040 [1]. Given the current market trends, it is evident that a substantial portion of this demand will be met by regional jet and single-aisle aircraft models such as the Embraer E190-E2, Airbus A320neo, and Boeing 737 MAX. Hence, the development of aerodynamically efficient designs for transonic aircraft is an integral step towards bringing down aircraft carbon emissions. A promising method for increasing aerodynamic efficiency is natural laminar flow (NLF), which delays the transition of a laminar boundary layer to reduce viscous drag [2]. Viscous drag constitutes roughly 50% of the overall drag of an aircraft [3], and the application of natural laminar flow to aircraft wings is estimated to have the potential to reduce aircraft-level drag by roughly 10% based on various NASA-sponsored studies and industry estimates [4].

Although NLF is a promising technology, its application has been limited to modest sweep angle and Reynolds number applications like nacelles and winglets [5]. In addition to significant operational challenges, there are two key design challenges in the application of NLF to transonic swept-wing aircraft. First, there are opposing pressure gradient requirements for suppressing Tollmien-Schlichting (TS) and crossflow (CF) instabilities, where a favourable pressure gradient suppresses TS waves but amplifies CF instabilities. Second, a design trade-off is required between reducing wave drag and viscous drag, where a high wing sweep angle reduces wave drag but amplifies CF instabilities, increasing viscous drag. However, a team at NASA Langley has recently demonstrated through wind tunnel experiments of the modified NASA Common Research Model (CRM) that significant NLF can potentially be achieved for high sweep angles and Reynolds numbers [6, 7]. The NASA-CRM wing was reshaped based on a crossflow-attenuated natural laminar

*Ph.D. Candidate, University of Toronto, AIAA Student Member, fizaa.husain@mail.utoronto.ca

†MAsc graduate, University of Toronto, current position: Aerodynamicist, Williams Racing, isabel.simmons@mail.utoronto.ca

‡University of Toronto Distinguished Professor of Computational Aerodynamics and Sustainable Aviation, Associate Fellow AIAA, david.zingg@utoronto.ca

flow method to suppress both CF and TS instabilities, with geometric constraints imposed to suppress attachment-line and Görtler instabilities [6, 7]. The results of these experiments demonstrate that significant drag reduction at a high Reynolds number of 15 million with a wing sweep of 37.3° is possible with NLF [7]. Furthermore, recent development of aerodynamic shape optimization algorithms coupled with transition prediction models has allowed aircraft designers to explore and address the inherent trade-offs required for achieving NLF on transonic aircraft. Numerous researchers have integrated optimization algorithms with either stability-based or transport-equation-based transition prediction methods to carry out NLF optimization. The following provides an overview of some of the relevant NLF optimization research.

Early efforts in the field of NLF optimization were focused on 2D airfoil design, with a primary goal of minimizing drag by delaying natural transition across subsonic regimes. Driver and Zingg [8] optimized NLF airfoils at subsonic conditions through the application of a Reynolds-averaged Navier-Stokes (RANS) based Newton-Krylov discrete-adjoint optimization algorithm. The transition prediction was performed with the MSES solver [9], which uses the simplified e^N method, and transition was enforced using trip terms of the Spalart-Allmaras (SA) turbulence model. Driver and Zingg were able to achieve airfoil shapes very similar to those designed by Liebeck [10]. Rashad and Zingg [11] coupled a 2D RANS based solver with an iterative transition prediction method based on the simplified e^N method [9] to perform gradient-based optimization of NLF airfoils. An intermittency function developed by Dhawan and Narasimha [12] was used to enforce transition and allow a more gradual initial ramp-up of the eddy-viscosity, resulting in a smoother design space and improved optimizer performance. Rashad and Zingg performed single-point optimizations at subsonic and transonic flight conditions to achieve NLF airfoils, followed by multipoint optimizations to ensure robustness of the optimized design to a range of operating conditions and uncertainties in the transition location. Shi et al. [13] performed NLF airfoil optimizations using the e^N method based on a database of linear stability theory results. The single-point optimizations were performed at subsonic flight conditions similar to those of the Cessna and HondaJet aircraft and resulted in optimized designs similar to Rashad and Zingg. A multipoint optimization was performed using flight conditions representative of the HondaJet aircraft to ensure robustness to perturbations in cruise conditions and acceptable performance at a nominal climb condition. Halila et al. [14] used the amplification factor transition model [15] to optimize NLF airfoils at subsonic and transonic conditions. A multipoint optimization was also performed at two coefficients of lift for the subsonic case to achieve a robust NLF airfoil design.

Recently, there has been an increased focus on addressing both TS and CF instabilities through infinite swept-wing optimization. Zhu and Qin [16] optimized a transonic infinite swept wing with and without shock bumps on the wing surface using an e^N transition criterion. The optimized wing with shock bumps had a lower sweep angle to suppress CF instabilities, and the shock bumps reduced the wave drag by moving shock formation further downstream, resulting in an overall reduction in aerodynamic drag. In addition, an aircraft-level assessment by Zhu and Qin of the optimized wing revealed that NLF design combined with shock bumps has the potential of reducing aircraft fuel consumption for a regional jet aircraft by 11.1% [17].

Shi et al. [18] extended their framework [13] to consider both TS and CF transition mechanisms and analyse infinite swept wing configurations at regional-jet flight conditions. The optimized wing section resulted in suppression of both CF and TS instabilities. Subsequently, Shi et al. [19] performed infinite swept-wing optimizations for NLF and HLFC configurations at operating conditions representative of the UW-5006 NLF wing and a regional jet aircraft. The study investigated the effect of Reynolds number, coefficient of lift, and sweep angle on NLF and HLFC design.

Sudhi et al. [20] used a genetic algorithm coupled with the MSES flow solver to optimize infinite swept-wing configurations for NLF and HLFC under mid-range aircraft operating conditions. A Pareto front was used for the optimization to study the trade-off between two design objectives which included maximizing the laminar flow region and minimizing pressure drag and suction drag. In addition, the inclusion of wing sweep as a design variable helped achieve a better optimum design than a fixed wing sweep optimization.

Sabater et al. [21] used a surrogate-based optimization method combined with an uncertainty quantification framework to optimize an infinite swept-wing configuration with operating conditions for a short-haul civil aircraft. The robust optimization framework takes into consideration uncertainties in environmental and operating conditions, using the mean value and 95 percent quantile of the drag as the objective functions. The robust design framework was able to achieve an NLF design with reliable performance for a wide range of operating conditions.

Han et al. [22] used a surrogate-based optimization method to analyse a transonic finite swept wing under regional-jet conditions. The baseline 3D wing used an optimized NLF airfoil as the wing section and a planform similar to the A320 aircraft wing. The baseline wing had a significant NLF region on the upper surface and a single-point optimization of this wing led to a weaker shock on the upper surface and an increase in the NLF region on the lower surface of the wing. The robustness of the optimized wing shape to uncertainties in the critical N factor, coefficient of lift, and Mach number

was also investigated. A multipoint optimization at two Mach numbers was then carried out to improve performance of the optimized design at lower than nominal Mach numbers.

The objective of the current work is to further investigate the application of aerodynamic shape optimization to swept NLF wings at transonic speed. Our interest is in the development of an effective methodology, the extent of laminar flow achievable for specific operating conditions, and the nature of the resulting wing designs. In particular, the Reynolds number and sweep angle associated with typical aircraft in the regional jet and single-aisle class are such that it is not clear that substantial amounts of laminar flow can be achieved.

II. Methodology

Aerodynamic shape optimization is performed using a high-fidelity aerodynamic shape optimization framework, Jetstream [23], which includes five main components: a Newton-Krylov-Schur flow solver for the RANS equations [24, 25], an empirical local correlation-based transition prediction model coupled to the Spalart-Allmaras (SA) turbulence model [26, 27], an integrated geometry parameterization and linear-elasticity-based mesh deformation scheme [28], a gradient-based optimizer SNOPT used with the discrete-adjoint gradient method [29], and a free-form and axial-curve deformation technique for geometry control [30].

A. RANS Flow Solver

The flow solver Diablo [24], is a multiblock parallel implicit solver that uses summation-by-parts (SBP) operators for spatial discretization and simultaneous approximation terms (SATs) for implementing boundary and block interface conditions. The SBP-SAT discretization of the governing equations results in a system of non-linear equations which is solved using Newton's method in two phases, an approximate-Newton phase followed by an inexact-Newton phase [31]. In the approximate-Newton phase, an approximate Jacobian is used with the implicit Euler method and the time step is increased slowly. In the inexact-Newton phase, the exact Jacobian is approximated through matrix-free matrix-vector products and the time step is increased more rapidly. A relative residual drop of five orders of magnitude in the total residual is used to switch from the approximate-Newton phase to the inexact-Newton phase for the current work. The system of linear equations generated at each iteration in both phases is solved using a preconditioned Krylov iterative solver GMRES.

B. Transition Prediction Model

1. SA-sLM2015cc Model

The flow solver includes the boundary-layer transition prediction capability using the SA-sLM2015cc model developed by Piotrowski and Zingg [26, 27]. The SA-sLM2015cc model is based on the $\gamma-Re_{\theta_t}$ model, an empirical local correlation-based model developed by Langtry and Menter [32, 33] for TS and CF instabilities. The $\gamma-Re_{\theta_t}$ model consists of two transport equations, one each for intermittency and the Reynolds momentum thickness number. Piotrowski and Zingg coupled this model with the one-equation SA turbulence model while maintaining a fully local formulation to create the SA-sLM2015 model [26]. The SA-sLM2015 model was smoothed by replacing stiff and non-smooth functions in the $\gamma-Re_{\theta_t}$ model to ensure a smooth design space and better numerical performance. Furthermore, the SA-sLM2015 model was recently extended by Piotrowski and Zingg [27] to include compressibility corrections for both TS and CF instabilities and is now designated as the SA-sLM2015cc model. This transition model has been validated previously by Piotrowski and Zingg with two and three dimensional subsonic [26] and transonic [27] transition test cases.

2. Crossflow Source-Term Activation

In the SA-sLM2015cc model, the crossflow source terms use helicity-based stationary crossflow correlations originally developed by Langtry [32]. These crossflow source terms produce a transition front for a swept wing that is dependent on the initialization of the flow field in a flow simulation. If the crossflow source terms are activated at the start of a flow simulation, they interfere with the natural transition process, causing a transition front to form upstream of the expected location [27]. Conversely, if the crossflow source terms are activated too late, this can result in flow separation upon encountering a shock, leading to convergence issues during a flow simulation.

To address these challenges and improve convergence while minimizing the impact on the final solution, a modification has been introduced to the activation of the crossflow source terms in the SA-sLM2015cc model. In the

original SA-sLM2015cc model, Piotrowski and Zingg used two conditions for activating crossflow source terms: the flow solver should be in the inexact-Newton phase and the solution update damping should be inactive [27]. For the current work, the source terms are activated in the approximate-Newton phase instead after only a relative residual drop of four orders of magnitude in the total residual and the second activation condition for solution update damping is not used. This modification improves convergence behaviour of the free-transition solution framework without affecting the converged result.

C. Geometry Parametrization, Mesh Deformation, Geometry Control, and Gradient-Based Optimization

The optimization framework consists of an integrated geometry parametrization and mesh deformation method developed by Hicken and Zingg [28] that is able to incorporate large geometry changes while maintaining grid quality, an analytical geometry representation, and low computational cost. Each block of the computational grid is associated with a B-spline volume, and the B-spline control points on the surface provide a low-dimensional approximation of the initial geometry. A linear-elasticity-based mesh deformation is applied to each B-spline volume to propagate changes to the volume control mesh based on the changes to the surface control points. Geometry control is achieved using a free-form and axial deformation method [30], where the free-form deformation (FFD) volumes are defined as B-spline volumes and the axial curves are defined as B-spline curves. In a wing optimization, the FFD volume control points are used to control section shape, chord and twist, while the axial curves are used to control sweep, span, and dihedral.

The aerodynamic shape optimization is performed using a gradient-based optimization algorithm, SNOPT [29], which uses a sequential quadratic programming framework and can handle both linear and non-linear constraints. The gradient of the objective function at each iteration of the optimization is evaluated using a discrete-adjoint method [28]. The flow adjoint equation is solved using a modified version of GCROT [34], while the mesh adjoint equations are solved using a preconditioned conjugate-gradient method.

D. Gradient-based Multistart Optimization

A gradient-based multistart (GBMS) method developed by Chernukhin and Zingg [35] and Streuber and Zingg [36] is used in Section III to investigate the design space of a 2D airfoil under Cessna172R design conditions. The GBMS method involves creating a set of initial geometries using the Sobol sampling method based on an initial baseline geometry. Each initial geometry is then independently optimized using the gradient-based optimizer SNOPT to an optimality tolerance of 1×10^{-6} . In addition, linear constraints are implemented during the sampling process to ensure that the initial geometries are feasible and realistic while still enabling thorough exploration of the design space.

In a previous study carried out by Piotrowski and Zingg [37] it was found that the design space for an airfoil under Cessna172R operating conditions is multimodal. Hence, a GBMS optimization is performed to further explore this design space to see if better local minima can be found. It is important to note that there are two differences in the optimization methodology used in the current analysis compared to the results presented previously by Piotrowski and Zingg [37]. First, in the current analysis the local pressure gradients for the transition model correlations are calculated using the Cartesian pressure gradients instead of the local Cartesian velocity gradients. This allows better agreement with experimental results and improves optimization convergence behaviour [38]. Second, a transition length modification developed by Piotrowski [38] is used that reduces the sensitivity of the transition source term to the transition onset criteria and the eddy viscosity to effectively increase the transition length of the model. Previously, Rashad and Zingg [11] demonstrated that increasing the transition length by slowing the increase in the eddy viscosity improves the smoothness of the design space, which is important for gradient-based optimization methods. Hence, the optimizations for the GBMS analysis are performed with this modification to allow for a smoother design space and more reliable convergence of the gradient-based optimizer.

E. Multipoint Optimization

A multipoint optimization is performed at a range of cruise conditions by varying Mach number and lift coefficient using the methodology developed by Buckley and Zingg [39]. The objective function for the multipoint optimization is a weighted integral of drag over a range of operating conditions subject to a lift constraint for each design point. The weighted integral is defined as [39]

$$\mathcal{J} = \int_{C_{L1}}^{C_{L2}} \int_{M1}^{M2} \mathcal{D}(M, C_L) C_D(M, C_L) dM dC_L \quad (1)$$

where \mathcal{D} are the user-defined weights used to put a greater emphasis on significant design points within a flight envelope. The weighted integral shown above can be approximated to obtain the following simplified multipoint objective function:

$$\mathcal{J} = \sum_{i=1}^N \mathcal{D}(M_i, C_{L_i}) C_D(M_i, C_{L_i}) \quad (2)$$

where N is the number of design points. This multipoint objective function is used in Section III to perform multipoint optimization.

III. Results

In this section, the free-transition optimization framework described in Section II is applied to single-point and multipoint optimizations of infinite swept and finite swept wings. Optimizations are performed for an infinite swept wing under typical cruise conditions for regional and business jet aircraft and for a finite wing under typical single-aisle aircraft cruise conditions. In addition, a multimodality analysis using the GBMS method is carried out to explore the design space for lift-constrained drag minimization of a low-speed airfoil under free-transition conditions.

A. Infinite Swept Wing Optimization

Optimizations are performed on a blunt-trailing edge RAE2822 geometry that is extruded one chord length to represent an infinite swept wing. The geometry is extruded at a sweep angle of 30° to ensure that both crossflow and Tollmien-Schlichting instabilities are captured. A structured multi-block O-type grid is used to model the infinite swept wing. Periodic boundary conditions are applied to the wing root and tip. The geometry is embedded within an FFD volume with 2 FFD-volume cross-sections at the wing root and tip, each consisting of 6 FFD-volume control point pairs. The wing root and tip control points are constrained to be equal, and the trailing-edge and leading-edge control points are constrained to symmetrical movement. The geometry also has one axial curve at the leading edge to enable sweep angle to be used as a design variable. Hence, there are effectively 11 geometric design variables plus angle of attack. Single-point and multipoint optimizations are carried out under typical cruise conditions for a regional jet and a business jet. During optimization, arbitrary minimum thickness constraints are enforced at each FFD volume control point pair. No cross-sectional area constraint is imposed.

1. Regional Jet

Lift-constrained drag minimization of the infinite swept wing is carried out at the operating conditions of the Embraer E190-E2 regional jet, which are a Mach number of 0.78, Reynolds number of 22×10^6 , and a target cruise lift coefficient of 0.47. A turbulence intensity of 0.10% and surface roughness of 1 μ inch are assumed for the transition parameters.

Single-point Optimization

A single-point optimization is performed for the infinite swept wing with a variable leading-edge sweep angle and with minimum thickness constraints enforced at each FFD volume control point pair. The chord is fixed while the section shape and angle of attack are allowed to vary within specified bounds. The baseline optimization problem is defined as

$$\begin{aligned} \min_{\mathbf{X}} \quad & C_D(\mathbf{X}), \\ \text{s.t.} \quad & C_L = 0.47, \\ & t/c \geq 0.725(t/c)_{\text{baseline}}. \end{aligned} \quad (3)$$

where \mathbf{X} represents the design variable vector, C_D and C_L represent coefficients of drag and lift, t/c is the thickness to chord ratio for each FFD control point pair, and the ‘baseline’ subscript is used to represent the value of the quantity from the initial geometry.

The results from this optimization are presented in Figure 1 and Table 1. Figure 1 shows a comparison between two different optimized cross-sectional profiles of the infinite swept wing against the initial design. The first optimization is conducted under fully-turbulent conditions without use of transition prediction. This optimized design was then analysed using transition prediction to show where transition would occur on a wing that has been optimized without laminar flow. The second optimization shown is optimized with the use of the transition-prediction methodology. The drag benefit

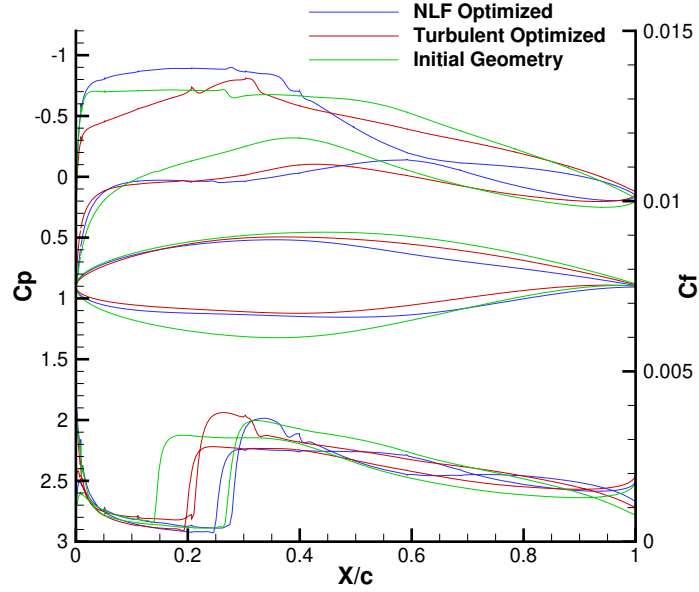


Fig. 1 Comparison of the initial, turbulent-optimized (analysed with free transition), and NLF-optimized designs produced by single-point optimization at a Reynolds number of 22×10^6 , Mach number of 0.78, and C_L of 0.47.

Table 1 Summary of results for optimization of an infinite swept wing at Mach 0.78 and Reynolds number 22×10^6 . $C_{D,p}$ is pressure drag, $C_{D,f}$ friction drag, AOA angle of attack, and Λ leading-edge sweep angle. Green and purple percentages represent overall drag reductions of the NLF-optimized design relative to the turbulent-optimized design and the turbulent-optimized design analyzed with free transition, respectively.

	C_D (cnts.)	$C_{D,p}$	$C_{D,f}$	C_L	C_M	L/D	AOA	Λ
Initial	61.75	23.15	38.60	0.47	-0.069	76.13	1.74°	30°
Optimized Turbulent	68.85	21.70	47.15	0.47	-0.065	68.27	1.46°	31.87°
Optimized Turbulent (Trans.)	57.27	18.26	39.01	0.47	-0.068	82.01	1.37°	31.87°
Optimized NLF (-24%, -8%)	52.47	16.56	35.91	0.47	-0.021	89.64	2.18°	27.04°
Optimized NLF (Fully-turb.)	70.65	24.50	46.15	0.47	-0.012	66.52	2.28°	27.04°

from the NLF-optimized design relative to the turbulent-optimized design under fully-turbulent conditions is 24% and relative to the turbulent-optimized design analysed with transition the benefit is 8%. This roughly translates to a 6%* overall aircraft drag reduction compared to the turbulent-optimized design analysed under fully-turbulent conditions.

In Figure 1, for the NLF-optimized shape it is seen that the optimizer is able to delay transition on both the upper and lower surfaces to 28% and 25% chord, respectively, by maintaining a near-zero pressure gradient on the upper surface and replacing the strong favourable pressure gradient on the lower surface with a near-zero pressure gradient. The turbulent-optimized design analyzed with transition has a mild favourable pressure gradient on the lower surface, causing transition further aft compared to the initial geometry. On the upper surface, the optimizer creates a strong favourable pressure gradient extending from the leading-edge to the quarter-chord causing earlier transition due to crossflow instabilities. With consideration of both Tollmien-Schlichting and crossflow instabilities, the optimizer is able to extend the laminar region on both surfaces of the NLF-optimized design, while retaining a weak shock comparable in strength to that seen on the turbulent-optimized design.

The NLF-optimized design is also analysed under fully-turbulent conditions in order to evaluate the decrease in

*Where wing profile drag is estimated to be roughly 25% of the total aircraft drag.

Table 2 Design conditions for each operating point in the multipoint optimization at regional-jet design conditions. All operating points are weighted equally.

Operating Point	Mach Number	C_L
1	0.78	0.47
2	0.78	0.49
3	0.78	0.45
4	0.76	0.47
5	0.80	0.47

performance of the optimized wing if transition occurs at the leading edge of the wing as opposed to the expected transition location, for example due to surface contamination. As shown in Table 1, this analysis resulted in a 34% increase in drag compared to the same design analysed with transition, but only a 2% increase compared to the turbulent-optimized design analysed under fully-turbulent conditions.

Multipoint Optimization

A multipoint optimization is performed to design a robust section shape for which performance does not deteriorate rapidly when operating at off-design conditions. In this case, the multipoint optimization is used to determine whether significant regions of laminar flow can still be maintained at conditions varying about the baseline. The baseline optimization problem is defined by Equation 3, with M_∞ and C_L values varied at each point according to Table 2. Each operating point is weighted equally.

In Table 3, comparing the NLF-optimized results to the turbulent-optimized results and the turbulent-optimized design analyzed with free transition shows a relatively consistent benefit at each operating point. There is a 22% benefit to optimizing for NLF instead of fully-turbulent conditions at each condition except for design point 4 where this benefit drops to 20%. The benefit from NLF optimization can be quantified by the drag reductions relative to the turbulent design analyzed with free transition. These are relatively consistent, with a marginally higher benefit at operating points 3 and 5, and a noticeably lower benefit at operating point 4.

The force and moment coefficients in Table 3 show a fairly consistent drag penalty at each design condition relative to the single-point optimizations except for condition 4, which shows a noticeably larger penalty. This could be due to premature crossflow transition due to operating at a higher than optimal sweep angle, or natural transition due to a shock. Although both scenarios are possible, when looking at the C_p , and C_f profiles of Figure 2d, we see that the shock on the upper surface has moved forward significantly relative to the single-point design. Therefore, it is likely that natural transition is the cause of premature transition at this design condition, as shocks tend to initiate natural transition. This premature transition causes a significantly higher increase in friction drag of 7% at this condition, relative to the next highest of 3% at design condition 3.

Figure 2 displays the cross-sectional, C_p , and C_f profiles of the NLF multipoint optimized results at each design condition with the corresponding single-point optimization results and the multipoint turbulent-optimized design analyzed with transition prediction. At each design condition for the the NLF and turbulent optimizations, the algorithm flattens the favourable pressure gradient on the lower surface in an attempt to delay the growth of crossflow instabilities. The gradients on both surfaces for the NLF multipoint results are more favourable than their corresponding single-point results, but less favourable than the corresponding turbulent multipoint results. This results in the transition location moving forward relative to the single-point results, and aftward relative to the turbulent multipoint results. All the NLF multipoint results except design condition 4 show the same delay of transition by roughly 6% chord on both surfaces relative to the turbulent multipoint optimization that was seen in the single-point case. This indicates that the benefit of NLF optimization relative to a turbulent-optimized design is maintained when designing for a range of off-design conditions.

Each result in the NLF multipoint optimization shows a lower pressure peak in exchange for more aft loading and a larger negative pitching moment relative to the corresponding single-point design. The optimization algorithm opts to reduce the strength of the shock and push it back in the multipoint case as a method of reducing pressure drag. The single-point optimizations show more significant reductions in pressure drag relative to friction drag as well; this is accomplished with heavy forward loading to maintain a near-zero pressure gradient while nearly eliminating the shock.

Table 3 Summary of results for the single-point and multipoint (MP) NLF optimizations, and fully turbulent multipoint optimizations with and without transition analysis. $C_{D,p}$ is pressure drag, $C_{D,f}$ friction drag, AOA angle of attack, and Λ leading-edge sweep angle. Green and purple percentages represent overall drag reductions of the NLF-optimized design relative to the turbulent-optimized design, and the turbulent-optimized design analyzed with free transition, respectively.

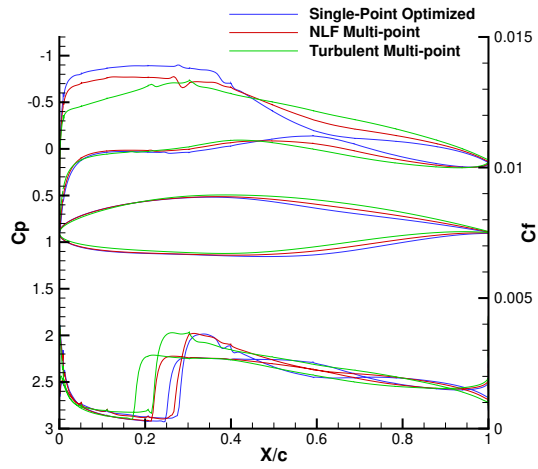
	C_D (cnts.)	$C_{D,p}$	$C_{D,f}$	C_L	C_M	L/D	Mach	AOA	Λ
Point1									
Single-Point NLF	52.47	16.56	35.91	0.47	-0.021	89.64	0.78	2.18°	27.04°
Turbulent MP	68.93	21.74	47.19	0.47	-0.069	68.18	0.78	1.47°	33.08°
Turbulent MP (Trans.)	58.02	18.43	39.59	0.47	-0.071	81.01	0.78	1.38°	33.08°
NLF MP (-22%, -7%)	53.67	16.66	37.01	0.47	-0.039	87.57	0.78	1.79°	29.36°
Point2									
Single-Point NLF	53.27	16.68	36.59	0.49	-0.021	91.93	0.78	2.27°	27.50°
Turbulent MP	70.01	22.93	47.08	0.49	-0.069	69.99	0.78	1.62°	33.08°
Turbulent MP (Trans.)	58.85	19.28	39.57	0.49	-0.071	83.26	0.78	1.52°	33.08°
NLF MP (-22%, -7%)	54.75	17.60	37.15	0.49	-0.038	89.50	0.78	1.93°	29.36°
Point3									
Single-Point NLF	51.70	15.75	35.95	0.45	-0.020	87.05	0.78	2.06°	26.51°
Turbulent MP	67.91	20.63	47.28	0.45	-0.069	66.26	0.78	1.32°	33.08°
Turbulent MP (Trans.)	57.24	17.66	39.58	0.45	-0.071	78.62	0.78	1.23°	33.08°
NLF MP (-22%, -8%)	52.68	15.88	36.80	0.45	-0.040	85.42	0.78	1.66°	29.36°
Point4									
Single-Point NLF	51.75	15.94	35.81	0.47	-0.029	90.82	0.76	2.00°	24.33°
Turbulent MP	68.62	21.16	47.46	0.47	-0.068	68.50	0.76	1.56°	33.08°
Turbulent MP (Trans.)	57.78	17.87	39.91	0.47	-0.070	81.35	0.76	1.47°	33.08°
NLF MP (-20%, -5%)	55.05	16.95	38.10	0.47	-0.038	85.37	0.76	1.92°	29.36°
Point5									
Single-Point NLF	53.37	17.03	36.34	0.47	-0.021	88.07	0.80	2.18°	28.71°
Turbulent MP	69.55	22.69	46.86	0.47	-0.070	67.58	0.80	1.37°	33.08°
Turbulent MP (Trans.)	58.70	19.48	39.22	0.47	-0.073	80.06	0.80	1.27°	33.08°
NLF MP (-22%, -8%)	54.23	17.68	36.55	0.47	-0.041	86.67	0.80	1.67°	29.36°

The benefit from NLF is generally maintained over a range of off-design conditions, and overall, NLF optimization is equally effective for the robust design obtained through multipoint optimization as for the single-point optimizations.

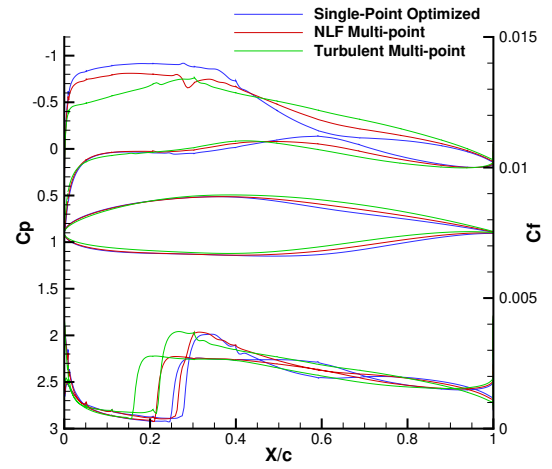
2. Business Jet

A high-speed single-point optimization is presented to investigate the extent of laminar flow that can potentially be maintained at higher Mach numbers and lower Reynolds numbers. The baseline design conditions, which are typical of a business jet, are given by Reist et al. [23]. These conditions are specified as a Mach number of 0.83, a Reynolds number of 13.5×10^6 , and a cruise lift coefficient of 0.35. A turbulence intensity of 0.10%, and a surface roughness of $1\mu\text{inch}$ are used. Sweep angle is active as a design variable. The optimization problem is defined as follows:

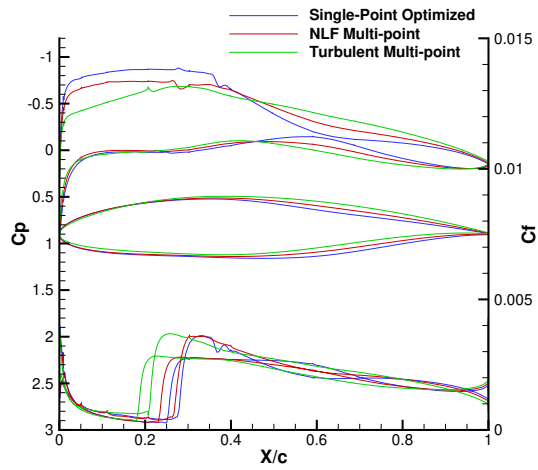
$$\begin{aligned}
 \min_{\mathbf{X}} \quad & C_D(\mathbf{X}), \\
 \text{s.t.} \quad & C_L = 0.35, \\
 & t/c \geq 0.85(t/c)_{\text{baseline}}.
 \end{aligned} \tag{4}$$



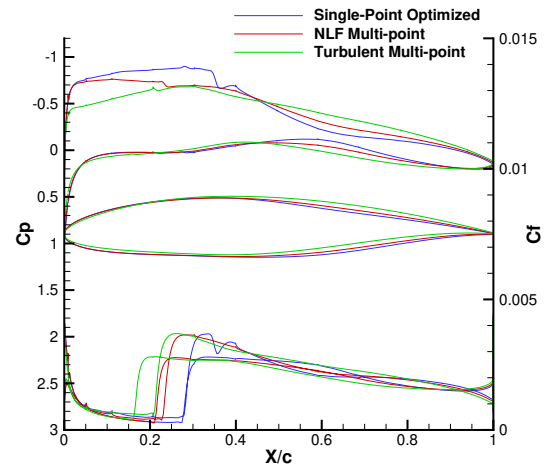
(a) Mach 0.78, $C_L = 0.47$



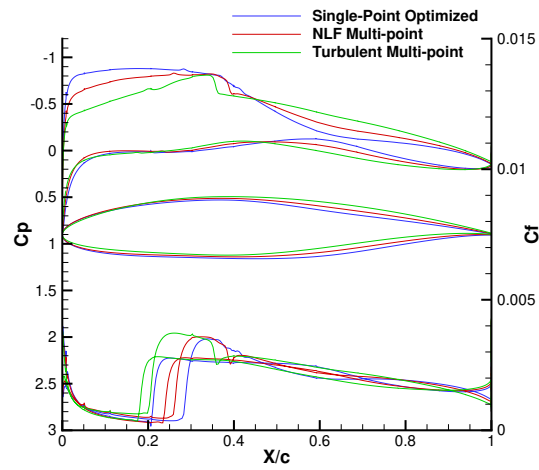
(b) Mach 0.78, $C_L = 0.49$



(c) Mach 0.78, $C_L = 0.45$



(d) Mach 0.76, $C_L = 0.47$



(e) Mach 0.80, $C_L = 0.47$

Fig. 2 Comparison of the multipoint NLF-optimized results against single point NLF-optimized results and the multipoint turbulent optimized design analyzed with free transition.

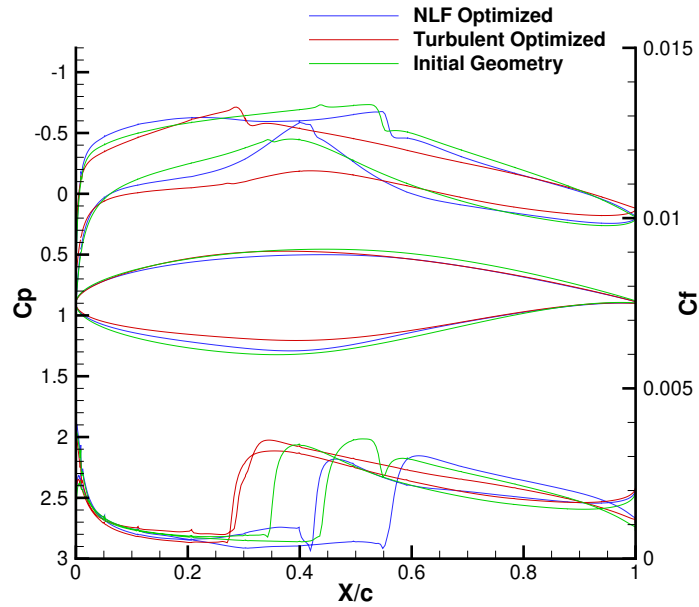


Fig. 3 Comparison of the initial, turbulent-optimized (analysed with free transition), and NLF-optimized designs produced by single-point optimization at a Reynolds number of 13.5×10^6 , Mach number of 0.83, and C_L of 0.35.

The C_p , C_f , and cross-sectional profiles of the NLF-optimized design, turbulent-optimized design analyzed with transition, and the initial geometry are presented in Figure 3. Similar to the previous section, fully-turbulent optimization results have been presented using a flow solution with transition prediction so that the transition location can be compared with the NLF results and the initial design. On the upper surface of the NLF-optimized design, the optimization algorithm has flattened out the favourable pressure gradient significantly and the shock has been pushed aft. This near-zero pressure gradient has allowed the optimizer to push transition on the upper surface from 28% chord on the turbulent-optimized geometry analyzed with transition, to 55% chord on the NLF-optimized airfoil. The pressure distribution created by the optimization algorithm on the lower surface was able to push transition aft from 27% chord on the turbulent-optimized design analyzed with transition to 42% chord on the NLF-optimized airfoil. The thickness constraint on the lower surface appears to be inactive in this case, showing that the optimization algorithm intentionally produces a steep favourable pressure gradient instead of a near-zero gradient. This is unusual based on trends observed in regional-jet results and by Piotrowski and Zingg [37]. At such a low Reynolds number, the local flow velocity on the lower surface relative to the upper surface is much lower and does not accelerate as quickly. As a result, the velocity is not high enough for crossflow instabilities to propagate, and the flow is not accelerating quickly enough to stabilize TS instabilities. These conditions make preventing natural transition more important; thus the optimization algorithm opts to create a strong favourable pressure gradient instead of a near-zero pressure gradient. In addition, the NLF-optimized design reduces the sweep angle from 30° to 28.38° , further suppressing crossflow instabilities.

The turbulent-optimized design shows a near-zero pressure gradient on the lower surface; this causes transition further forward from the initial location. Given the extremely high sweep angle, it is likely that crossflow instabilities are exacerbated and lead to premature transition. The turbulent-optimized design maintains a strong favourable pressure gradient on the upper surface and the shock has moved forward from approximately 44% chord on the initial design to 30% chord on the turbulent design. As a result, transition is pushed forward relative to its initial location. The turbulent-optimized airfoil analyzed with transition actually has higher drag than the initial geometry, which is not unexpected, as the optimization was performed under fully-turbulent conditions.

The forces and moments are presented in Table 4. The NLF-optimized design shows a 40% reduction in overall drag relative to the turbulent-optimized design and a 25% reduction relative to the turbulent-optimized design analyzed with free transition. This roughly translates to a 10% reduction in overall aircraft drag compared to the turbulent-optimized

Table 4 Summary of results for optimization of an infinite swept wing at Mach 0.83 and Reynolds number 13.5×10^6 . $C_{D,p}$ is pressure drag, $C_{D,f}$ friction drag, AOA angle of attack, and Λ leading-edge sweep angle. Green and purple percentages represent overall drag reductions of the NLF-optimized design relative to the turbulent-optimized design, and the turbulent-optimized design analyzed with free transition, respectively.

	C_D (cnts.)	$C_{D,p}$	$C_{D,f}$	C_L	C_M	L/D	AOA	Λ
Initial	50.46	17.36	33.10	0.35	-0.076	69.37	0.65°	30°
Optimized Turbulent	68.43	18.53	49.90	0.35	-0.047	51.15	1.16°	40.61°
Optimized Turbulent (Trans.)	54.68	16.25	38.43	0.35	-0.051	64.00	1.03°	40.61°
Optimized NLF (-40%, -25%)	41.07	12.05	29.02	0.35	-0.066	85.22	0.72°	28.38°
Optimized NLF (Fully-turb.)	75.20	25.77	49.43	0.35	-0.058	46.55	1.01°	28.38°

case analysed under fully-turbulent conditions. A greater drag reduction is achieved for the infinite swept wing under business-jet conditions compared to the regional-jet conditions because of the lower design Reynolds number. The NLF-optimized design shows significant reductions in both pressure drag and friction drag relative to the turbulent-optimized design. The pressure drag reduction comes from both a reduction of the shock strength on the upper surface and the aftward movement of the transition points, while the friction drag reduction can be attributed to a significant extension of the laminar boundary layer on both surfaces.

The NLF-optimized design is also analysed under fully-turbulent conditions, resulting in an 83% increase in drag compared to the same design analysed with transition and a 10% increase compared to the turbulent-optimized design analysed under fully-turbulent conditions. This drag penalty is much higher than the regional jet case and highlights the importance of considering fully-turbulent performance during NLF optimization, as previously shown by Rashad and Zingg [11], which will be addressed in future work.

B. Finite-Wing Optimization - Single-aisle Aircraft

1. Single-point Optimization

A wing with the RAE2822 airfoil section shape and a planform similar to the Airbus A320neo wing without winglets is used as the initial geometry. The wing has a half span of 59 feet, a mean aerodynamic chord of 14.4 feet, and a leading edge sweep angle of 28.36°. The grid is a structured multi-block O-topology grid. The geometry is embedded within an FFD volume with 9 FFD-volume cross-sections, each consisting of 11 FFD-volume control point pairs. The axial curves are positioned at the leading edge of the wing. The wing planform and the FFD volume and control points are illustrated in Figure 4. The operating conditions for the optimization are chosen to represent typical cruise conditions of a single-aisle aircraft. These are specified as a Mach number of 0.78, a Reynolds number of 27×10^6 , and a lift coefficient of 0.5. A freestream turbulence intensity of 0.07% and a surface roughness of 1 μm is assumed.

A lift-constrained drag minimization is performed with minimum thickness constraints enforced at each FFD volume control point pair and a minimum wing volume constraint. The span, chord, and sweep angle of the wing are fixed, while the wing thickness, twist, and angle of attack are allowed to vary within specified bounds. The optimization problem is given by,

$$\begin{aligned}
 \min_{\mathbf{X}} \quad & C_D(\mathbf{X}), \\
 \text{s.t.} \quad & C_L = 0.50, \\
 & V \geq V_{\text{baseline}}, \\
 & t/c \geq 0.75(t/c)_{\text{baseline}}.
 \end{aligned} \tag{5}$$

where \mathbf{X} represents the design variable vector, C_D and C_L represent coefficients of drag and lift, V is the wing volume, t/c is the thickness to chord ratio for each FFD control point pair, and the ‘baseline’ subscript denotes the value of the quantity from the initial geometry.

Force and moment coefficients are presented in Table 5, with transition fronts shown in Figure 5 and sectional shapes and pressure distributions in Figure 6. Table 5 presents results for the initial wing, a wing optimized and analyzed under fully-turbulent conditions, the same wing analyzed with transition prediction, and the wing optimized and analyzed

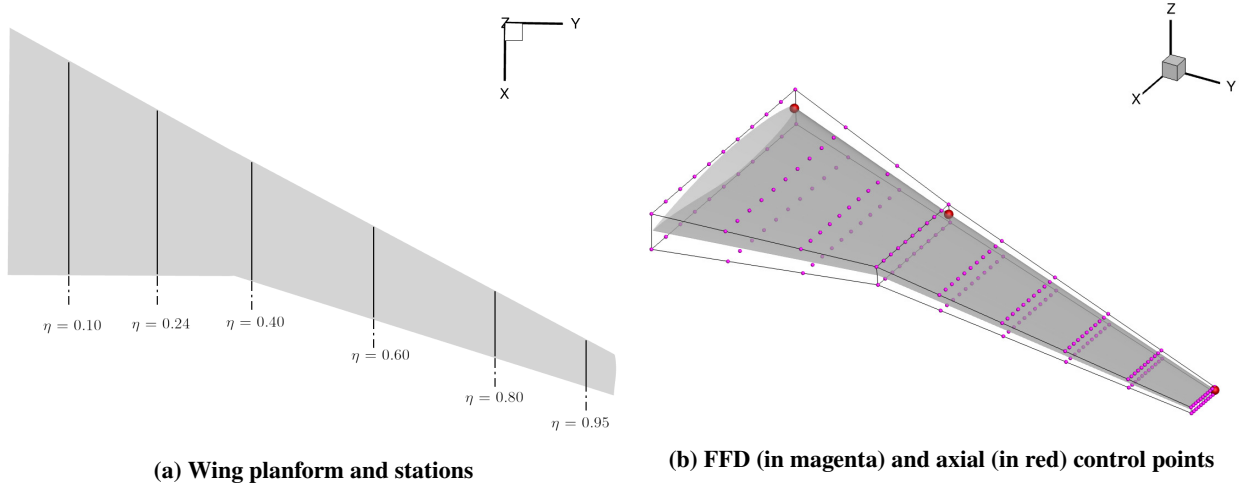


Fig. 4 The single-aisle aircraft wing planform (left) and the FFD control points and axial control points for the geometry control (right).

Table 5 Summary of results for optimization of a single-aisle aircraft wing at Mach 0.78 and Reynolds number 27×10^6 . $C_{D,p}$ is pressure drag, $C_{D,f}$ friction drag, and AOA angle of attack. Green and purple percentages represent overall drag reductions of the NLF-optimized design relative to the turbulent-optimized design, and the turbulent-optimized design analyzed with free transition, respectively.

	$C_D(\text{cnts.})$	$C_{D,p}$	$C_{D,f}$	C_L	C_M	L/D	AOA
Initial	169.3	128.8	40.5	0.5	-0.224	29.5	2.18°
Optimized Turbulent	149.4	101.8	47.6	0.5	-0.213	33.4	2.36°
Optimized Turbulent (Trans.)	139.0	98.2	40.8	0.5	-0.218	36.0	2.25°
Optimized NLF (-10%, -4%)	134.0	97.4	36.5	0.5	-0.214	37.3	1.98°

with transition prediction. The optimizer has successfully been able to push the transition front further aft, balancing TS and CF instabilities and reducing drag by 10% relative to a turbulent-optimized geometry and by 4% relative to a turbulent-optimized geometry analysed with free transition. This roughly translates to a 5%[†] overall aircraft drag reduction compared to the turbulent-optimized case analyzed under fully-turbulent conditions.

Figure 6 shows that near the root of the wing at $\eta = 0.1$ and 0.24 for the NLF-optimized wing there is a significant improvement in the transition front on the upper surface of the wing while the lower surface transition front changes by only a small amount. On the upper surface, the rapid acceleration close to the leading edge followed by a favourable pressure gradient helps suppress both CF and TS instabilities and pushes the transition location further downstream. However, the lower surface is dominated by the crossflow instabilities close to the leading edge, as the optimizer is unable to avoid a favourable pressure gradient in this region. On the outboard half of the wing beyond $\eta = 0.4$, the optimizer is able to make significant improvements to the location of transition on both surfaces of the wing. For the optimized shape there is a near-zero pressure gradient on the upper surface, pushing the transition front further aft. The optimizer is also able to replace the favourable pressure gradient close to the leading edge of the wing on the lower surface with a more neutral pressure gradient by introducing a convex cut on the lower surface which can be seen in Figures 6c, 6d, and 6e. This helps suppress crossflow instabilities that are dominant at the leading edge of the wing and pushes the transition front further aft. There is also a negative twist imposed by the optimizer on the outboard half of the wing which increases gradually closer to the tip of the wing. The negative twist helps reduce the C_p peak on the upper surface and reduces the strong adverse pressure gradients closer to the leading edge, maintaining a near-zero pressure gradient and resulting in a weaker shock compared to the initial geometry. Hence, reductions in both wave drag

[†] Where wing drag, including induced drag, is estimated to be roughly 50% of the total aircraft drag.

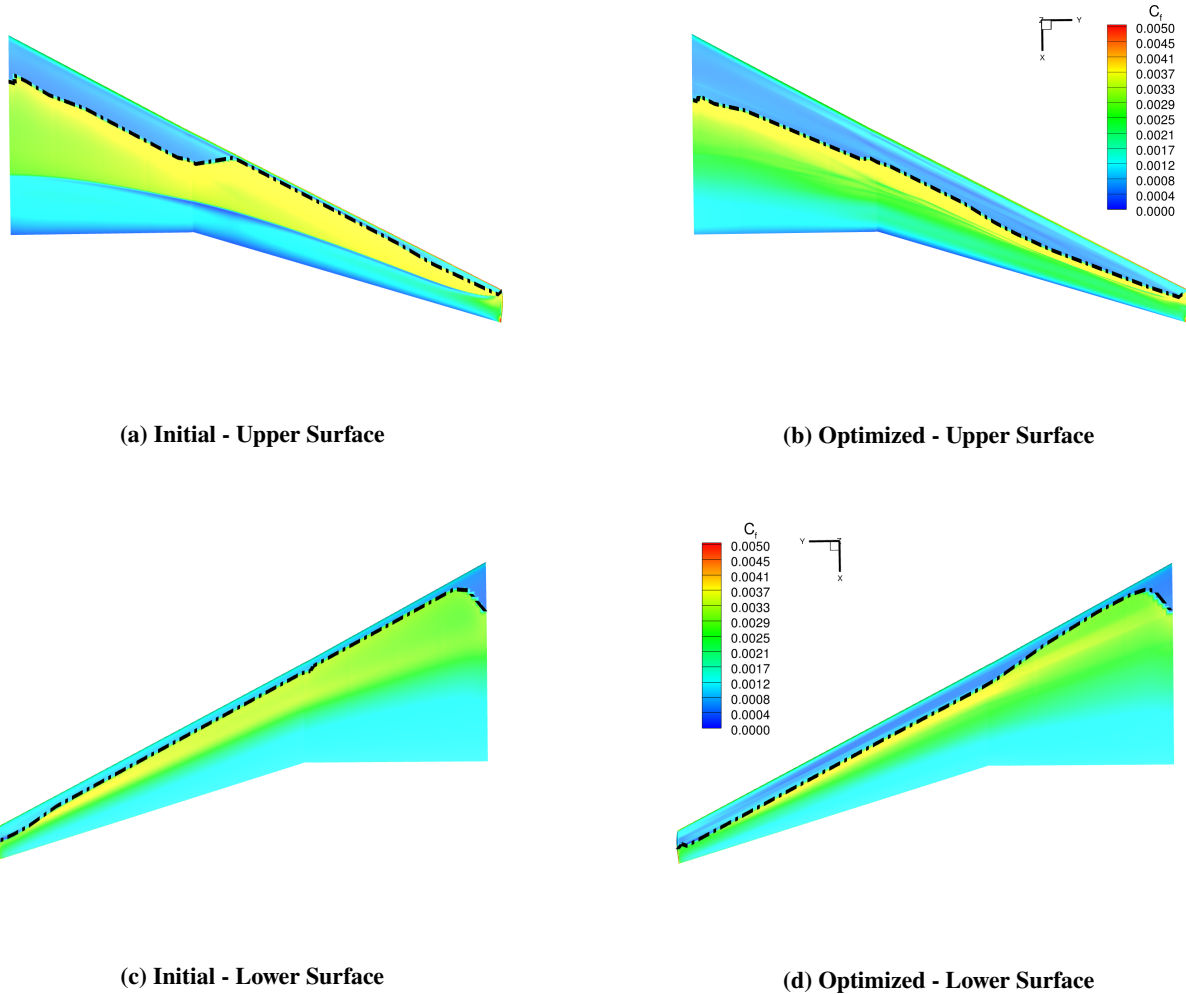


Fig. 5 Comparison of the initial and optimized C_f contours for the upper (top row) and lower (bottom row) surfaces of the single-aisle aircraft wing produced by single-point optimization with fixed wing sweep of 28.36° . The dash-dot line shows the location of transition.

and viscous drag contribute to the overall drag reduction.

C. Airfoil Optimization - Multimodal Analysis

A GBMS optimization is performed for an airfoil under typical cruise conditions for a Cessna 172R Skyhawk. These design conditions are specified as a Mach number of 0.19, Reynolds number of 5.6×10^6 , and a target coefficient of lift of 0.30. A turbulence intensity of 0.07% is used for the transition model parameter. A structured multi-block O-type topology grid around the RAE2822 airfoil is used as the baseline grid. The airfoil geometry is embedded within a FFD volume with 6 streamwise FFD-volume control points each for the upper and lower surface of the airfoil. The RAE2822 airfoil is the baseline configuration for defining geometric constraints, and the Sobol method is used to create a set of 20 samples. The set of 20 initial geometries plus the baseline configuration are shown in Figure 7.

Lift-constrained drag minimizations are carried out independently for each sample and the baseline geometry with loose minimum thickness constraints enforced at each FFD volume control point pair and a minimum airfoil cross-sectional area constraint. The optimization problem for each sample is defined as

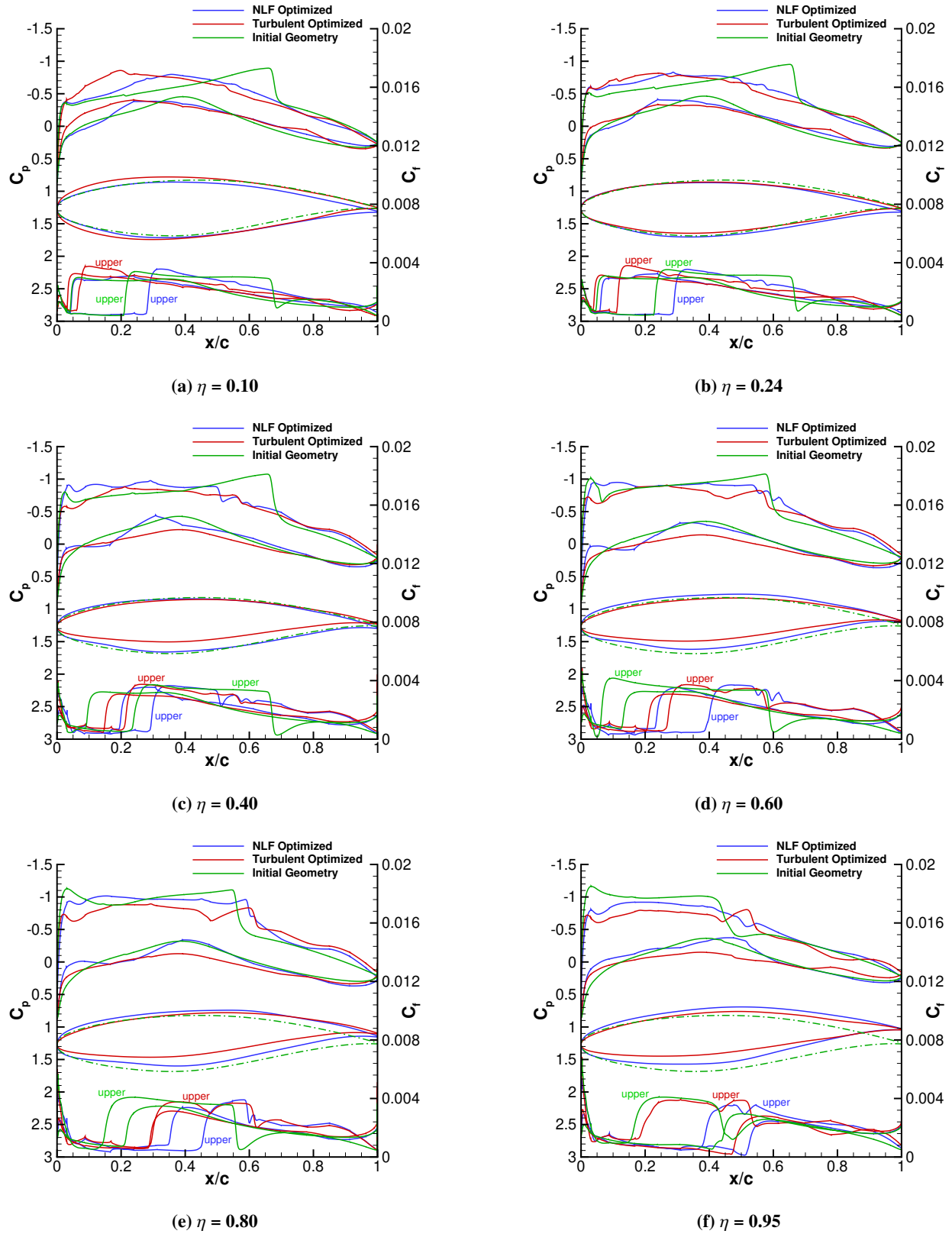


Fig. 6 Comparison of the initial, turbulent-optimized (analysed with free transition) and NLF-optimized designs at 6 wing stations produced by single-point optimization of a single-aisle aircraft wing at a Reynolds number of 27×10^6 , Mach number of 0.78 and C_L of 0.50.

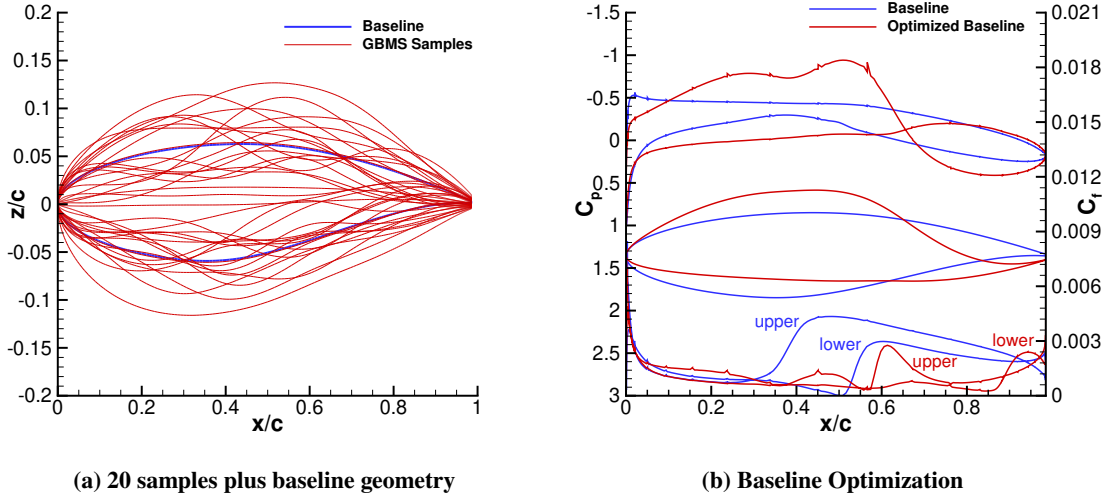


Fig. 7 The 20 initial samples for the GBMS optimization created using the Sobol method (left) and the baseline optimization results for the Cessna172R design conditions (right).

Table 6 Summary of GBMS optimization results of the RAE2822 airfoil under Cessna172R design conditions

	C_L	C_D (cnts.)	C_M	L/D	% decrease in C_D	# of samples
Baseline	0.30	49.57	-0.061	60.78	-	-
Optimized Baseline	0.30	28.56	0.043	105.1	-42%	-
Optimum 1	0.30	28.56	0.049	105.1	-42%	7
Optimum 2	0.30	27.47	-0.069	109.2	-44%	13

$$\begin{aligned}
 & \min_{\mathbf{X}} C_D(\mathbf{X}), \\
 & \text{s.t. } C_L = 0.30, \\
 & A \geq A_{\text{baseline}}, \\
 & t/c \geq 0.15(t/c)_{\text{baseline}}.
 \end{aligned} \tag{6}$$

where \mathbf{X} represents the design variable vector, C_D and C_L represent coefficients of drag and lift, A is the cross-sectional area of the airfoil, t/c is the thickness to chord ratio for each FFD control point pair, and the ‘baseline’ subscript is used to represent the value of the quantity from the initial geometry.

The optimization results for the baseline geometry are summarized in Figure 7b and Table 6. The baseline optimization gives a drag reduction of 42% relative to the initial geometry by delaying transition to approximately 55% and 85% chord on the upper and lower surfaces, respectively. In the optimized shape a mild favourable pressure gradient is maintained on the upper surface to suppress TS instabilities, with transition eventually occurring in a strong adverse pressure gradient. On the lower surface the optimizer is again able to create a mild favourable pressure gradient that pushes transition much further aft on the lower surface relative to the baseline configuration. The optimizer achieves this with a higher angle of attack relative to baseline, decreased trailing edge thickness, and a more forward loaded design. A strong adverse pressure gradient is also introduced after the transition location on the upper surface by thinning the wing in order to reduce skin friction drag in the turbulent region.

Optimization of the 20 samples resulted in 2 distinct local optima, differentiated based on their final shapes, transition locations, and aerodynamic performance. The results for each local optimum are summarized in Table 6 with the final shapes and C_p - C_f plots presented in Figure 8. The first local optimum is the same as the baseline optimized shape, whereas the second produces 3.8% lower drag, significantly pushing the transition front aft to 70% chord on both the

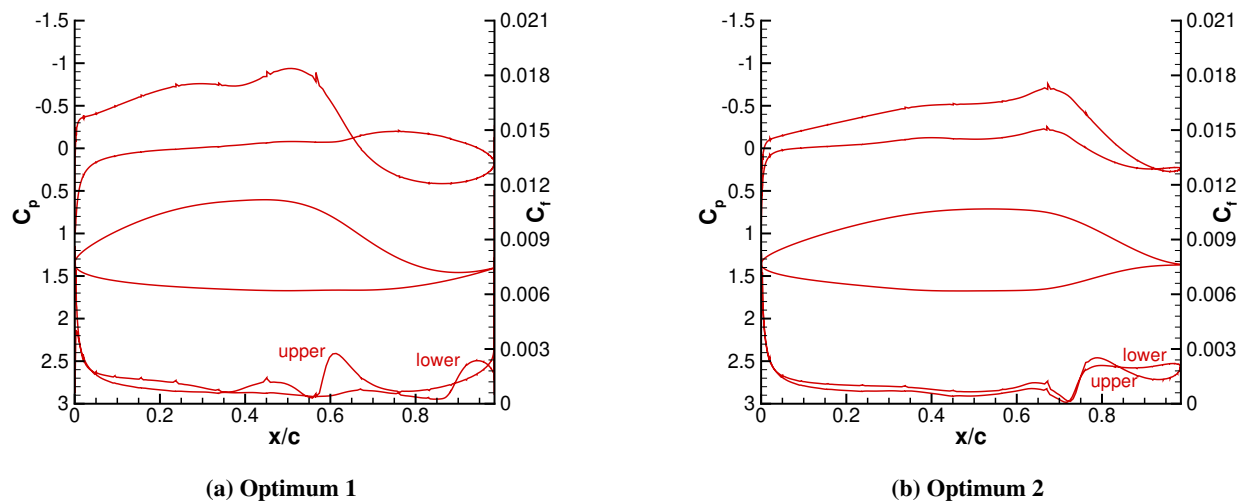


Fig. 8 Cross-sectional, C_p , and C_f profiles of 2 local optima from the GBMS optimization under free-transition conditions.

upper and lower surfaces. For the second local optimum shape, there is a near-zero pressure gradient on both the upper and lower surface and more aft loading compared to the baseline optimization.

These results demonstrate the effectiveness of the GBMS method in identifying local minima and potentially the global minimum in a design space. Despite the limited exploration of the design space with only 20 initial samples, the analysis identified two local minima. While the possibility of additional local minima cannot be discounted, the second optimum has emerged as the best performing optimized shape so far. In addition, these two optima correspond to shapes previously identified by Piotrowski and Zingg [37], where a shape similar to the second optimum was achieved by implementing additional constraints on the optimization based on prior knowledge, namely the airfoil geometry achieved by Rashad and Zingg [11] for the same case. Using GBMS the preferred optimum was found without exploiting any prior knowledge.

A GBMS optimization is also carried out under fully-turbulent conditions using the optimization problem defined by Equation 6, and the design space is found to be unimodal. All 20 initial samples, including the baseline configuration, converged to a single optimum, shown in Figure 9. In addition, Chernukhin and Zingg [35] previously conducted GBMS optimizations for airfoils under fully-turbulent conditions across Mach numbers ranging from 0.5 to 0.85, revealing no evidence of multimodality. Hence, these results suggest that multimodality may be a more significant concern for optimizations performed under free-transition conditions.

IV. Conclusions

In this paper, we present a framework for aerodynamic shape optimization aimed at delaying boundary-layer transition on swept wings operating at transonic speeds. Our study includes both infinite swept-wing optimizations, performed at design conditions of business and regional jet aircraft with variable leading-edge sweep angles, and finite-wing optimizations performed at a single-aisle aircraft conditions with a fixed wing sweep.

The results for the infinite swept wing demonstrate that the free-transition optimization framework is effective in delaying boundary-layer transition by suppressing both crossflow and Tollmien-Schlichting instabilities. By introducing near-zero pressure gradients on both the upper and lower surfaces the transition front is pushed further aft resulting in approximately 6% and 10% aircraft drag reduction relative to a turbulent-optimized shape analysed fully turbulent for the regional and business jet conditions, respectively. Multipoint optimization performed for the infinite swept wing at regional-jet conditions reveals that the design is not sensitive to changes in Mach number and coefficient of lift, and the benefits from NLF are maintained over a range of operating conditions.

For finite wings the optimizer achieves similar success by reducing leading-edge radius and incorporating convex cuts on the lower surface to reduce strong favourable pressure gradients and delay boundary-layer transition. In addition,

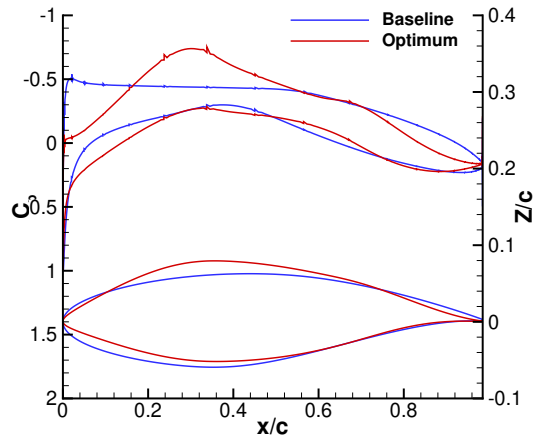


Fig. 9 Comparison of the C_p and C_f profile of the baseline and optimum from the GBMS optimization under fully-turbulent conditions.

the optimizer is able to reduce shock strength by reducing the favourable pressure gradients on the upper surface of the wing. Hence, the optimizer is able to reduce overall aircraft drag by approximately 5% relative to a turbulent-optimized shape analysed fully turbulent.

Finally, the GBMS optimization of a low-speed airfoil under free-transition conditions reveals two distinct local minima, whereas under fully-turbulent conditions, only one local minimum is found. These results highlight the significance of addressing multimodality in the design spaces of free-transition optimization.

Acknowledgments

This work is partially funded by Bombardier, Transport Canada, the Natural Sciences and Engineering Research Council (NSERC), the Kenneth M. Molson Foundation, and the University of Toronto. All results in this paper were computed on the Niagara supercomputer at the SciNet HPC Consortium, a part of Compute Canada.

References

- [1] International Civil Aviation Organization Council, "Annual Report 2019," 2019. URL <https://www.icao.int/annual-report-2019>.
- [2] Green, J. E., "Civil Aviation and the Environment—The Next Frontier for the Aerodynamicist," *The Aeronautical Journal*, Vol. 110, No. 1110, 2006, pp. 469–486.
- [3] Bushnell, D. B., "Overview of Aircraft Drag Reduction Technology," *AGARD Report 786 (Special Course on Skin Friction Drag Reduction)*, 1992.
- [4] Malik, M. R., Crouch, J. D., Saric, W. S., Lin, J. C., and Whalen, E. A., "Application of Drag Reduction Techniques to Transport Aircraft," *In Encyclopedia of Aerospace Engineering*, 2015.
- [5] Crouch, J., "Boundary-layer Transition Prediction for Laminar Flow Control," *45th AIAA Fluid Dynamics Conference*, AIAA Paper 2015–2472, Dallas, TX, 2015.
- [6] Lynde, M. N., and Campbell, R. L., "Computational Design and Analysis of a Transonic Natural Laminar Flow Wing for a Wind Tunnel Model," *35th AIAA Applied Aerodynamics Conference*, AIAA Paper 2017–3058, Denver, CO, 2017.
- [7] Lynde, M. N., Campbell, R. L., Rivers, M. B., Viken, S. A., Chan, D. T., Watkins, A. N., and Goodliff, S. L., "Preliminary Results from an Experimental Assessment of a Natural Laminar Flow Design Method," *AIAA Scitech 2019 Forum*, AIAA Paper 2019–2298, 2019.
- [8] Driver, J., and Zingg, D. W., "Numerical Aerodynamic Optimization Incorporating Laminar-Turbulent Transition Prediction," *AIAA Journal*, Vol. 45, No. 8, 2007, pp. 1810–1818.

- [9] Drela, M., and Giles, M. B., “Viscous-inviscid Analysis of Transonic and Low Reynolds Number Airfoils,” *AIAA Journal*, Vol. 25, No. 10, 1987, pp. 1347–1355.
- [10] Liebeck, R. H., “A Class of Airfoils Designed for High Lift in Incompressible Flow,” *Journal of Aircraft*, Vol. 10, No. 10, 1973, pp. 610–617.
- [11] Rashad, R., and Zingg, D. W., “Aerodynamic Shape Optimization for Natural Laminar Flow Using a Discrete-Adjoint Approach,” *AIAA Journal*, Vol. 54, No. 11, 2016, pp. 3321–3337.
- [12] Dhawan, S., and Narasimha, R., “Some Properties of Boundary Layer Flow during the Transition from Laminar to Turbulent Motion,” *Journal of Fluid Mechanics*, Vol. 3, No. 4, 1958, p. 418–436.
- [13] Shi, Y., Mader, C. A., He, S., Halila, G. L. O., and Martins, J. R. R. A., “Natural Laminar-Flow Airfoil Optimization Design Using a Discrete Adjoint Approach,” *AIAA Journal*, Vol. 58, No. 11, 2020, pp. 4702–4722.
- [14] Halila, G. L., Martins, J. R., and Fidkowski, K. J., “Adjoint-based Aerodynamic Shape Optimization including Transition to Turbulence Effects,” *Aerospace Science and Technology*, Vol. 107, 2020, pp. 1–15.
- [15] Coder, J. G., and Maughmer, M. D., “Computational Fluid Dynamics Compatible Transition Modeling Using an Amplification Factor Transport Equation,” *AIAA Journal*, Vol. 52, No. 11, 2014, pp. 2506–2512.
- [16] Zhu, M., and Qin, N., “Balancing Laminar Extension and Wave Drag for Transonic Swept Wings,” *AIAA Journal*, Vol. 59, No. 5, 2021, pp. 1660–1672.
- [17] Fan, Z., Yu, X., Qin, N., and Zhu, M., “Benefit Assessment of Low-Sweep Transonic Natural Laminar Flow Wing for Commercial Aircraft,” *Journal of Aircraft*, Vol. 58, No. 6, 2021, pp. 1294–1301.
- [18] Shi, Y., Mader, C. A., and Martins, J., “Natural Laminar Flow Wing Optimization using a Discrete Adjoint Approach,” *Structural and Multidisciplinary Optimization*, Vol. 64, No. 2, 2021, pp. 541–562.
- [19] Shi, Y., Lan, X., and Yang, T., “Hybrid Laminar Flow Control Optimizations for Infinite Swept Wings,” *International Journal of Aerospace Engineering*, Vol. 2023, 2023, pp. 1–33.
- [20] Sudhi, A., Radespiel, R., and Badrya, C., “Design Exploration of Transonic Airfoils for Natural and Hybrid Laminar Flow Control Applications,” *Journal of Aircraft*, Vol. 60, No. 3, 2023, pp. 716–732.
- [21] Sabater, C., Bekemeyer, P., and Görtz, S., “Robust Design of Transonic Natural Laminar Flow Wings under Environmental and Operational Uncertainties,” *AIAA Scitech 2021 Forum*, 2021.
- [22] Han, Z., Chen, J., Zhang, K., Xu, Z., Zhu, Z., and Song, W., “Aerodynamic Shape Optimization of Natural-Laminar-Flow Wing Using Surrogate-Based Approach,” *AIAA Journal*, Vol. 56, No. 7, 2018, pp. 2579–2593.
- [23] Reist, T. A., Koo, D., Zingg, D. W., Bochud, P., Castonguay, P., and Leblond, D., “Cross Validation of Aerodynamic Shape Optimization Methodologies for Aircraft Wing-Body Optimization,” *AIAA Journal*, Vol. 58, No. 6, 2020, pp. 2581–2595.
- [24] Osusky, M., and Zingg, D. W., “Parallel Newton–Krylov–Schur Flow Solver for the Navier–Stokes Equations,” *AIAA Journal*, Vol. 51, No. 12, 2013, pp. 2833–2851.
- [25] Osusky, L., Buckley, H., Reist, T., and Zingg, D. W., “Drag Minimization Based on the Navier–Stokes Equations Using a Newton–Krylov Approach,” *AIAA Journal*, Vol. 53, No. 6, 2015, pp. 1555–1577.
- [26] Piotrowski, M. G. H., and Zingg, D. W., “Smooth Local Correlation-Based Transition Model for the Spalart–Allmaras Turbulence Model,” *AIAA Journal*, Vol. 59, No. 2, 2021, pp. 474–492.
- [27] Piotrowski, M. G. H., and Zingg, D. W., “Compressibility Corrections to Extend a Smooth Local Correlation-based Transition Model to Transonic Flows,” *The Aeronautical Journal*, Vol. 127, No. 1313, 2023, pp. 1141–1170.
- [28] Hicken, J. E., and Zingg, D. W., “Aerodynamic Optimization Algorithm with Integrated Geometry Parameterization and Mesh Movement,” *AIAA Journal*, Vol. 48, No. 2, 2010, pp. 400–413.
- [29] Gill, P. E., Murray, W., and Saunders, M. A., “SNOPT: An SQP Algorithm for Large-Scale Constrained Optimization,” *SIAM Journal on Optimization*, Vol. 12, No. 4, 2002, pp. 979–1006.
- [30] Gagnon, H., and Zingg, D., “Two-Level Free-Form and Axial Deformation for Exploratory Aerodynamic Shape Optimization,” *AIAA Journal*, Vol. 53, No. 7, 2015, pp. 2015–2026.

- [31] Chisholm, T. T., and Zingg, D. W., "A Newton-Krylov Algorithm for Turbulent Aerodynamic Flows," *41st AIAA Aerospace Sciences Meeting and Exhibit*, AIAA Paper 2003-0071, Reno, Nevada, 2003.
- [32] Langtry, R. B., "Extending the γ - $Re_{\theta t}$ Correlation based Transition Model for Crossflow Effects," *45th AIAA fluid dynamics conference*, AIAA Paper 2015-2474, 2015.
- [33] Langtry, R. B., and Menter, F. R., "Correlation-based Transition Modeling for Unstructured Parallelized Computational Fluid Dynamics Codes," *AIAA journal*, Vol. 47, No. 12, 2009, pp. 2894–2906.
- [34] Hicken, J., and Zingg, D., "A Simplified and Flexible Variant of GCROT for Solving Nonsymmetric Linear Systems," *SIAM J. Scientific Computing*, Vol. 32, 2010, pp. 1672–1694.
- [35] Chernukhin, O., and Zingg, D. W., "Multimodality and Global Optimization in Aerodynamic Design," *AIAA Journal*, Vol. 51, No. 6, 2013, pp. 1342–1354.
- [36] Streuber, G. M., and Zingg, D. W., "Investigation of Multimodality in Aerodynamic Shape Optimization Based on the Reynolds Averaged Navier-Stokes Equations," *35th AIAA Applied Aerodynamics Conference*, AIAA Paper 2017-3752, 2017.
- [37] Piotrowski, M. G., and Zingg, D. W., "Investigation of a Smooth Local Correlation-based Transition Model in a Discrete-Adjoint Aerodynamic Shape Optimization Algorithm," *AIAA Scitech 2022 Forum*, 2022.
- [38] Piotrowski, M. G., "Development of a Transition Prediction Methodology Suitable for Aerodynamic Shape Optimization," Ph.D. thesis, University of Toronto, Toronto, Canada, 2022.
- [39] Buckley, H. P., and Zingg, D. W., "Approach to Aerodynamic Design Through Numerical Optimization," *AIAA Journal*, Vol. 51, No. 8, 2013, pp. 1972–1981.